Manifold Bootstrapping for SVBRDF Capture

Yue Dong [*†]   Jiaping Wang[†]   Xin Tong[†]   John Snyder[‡]   Moshe Ben-Ezra [†]   Yanxiang Lan [*†]   Baining Guo [†*]

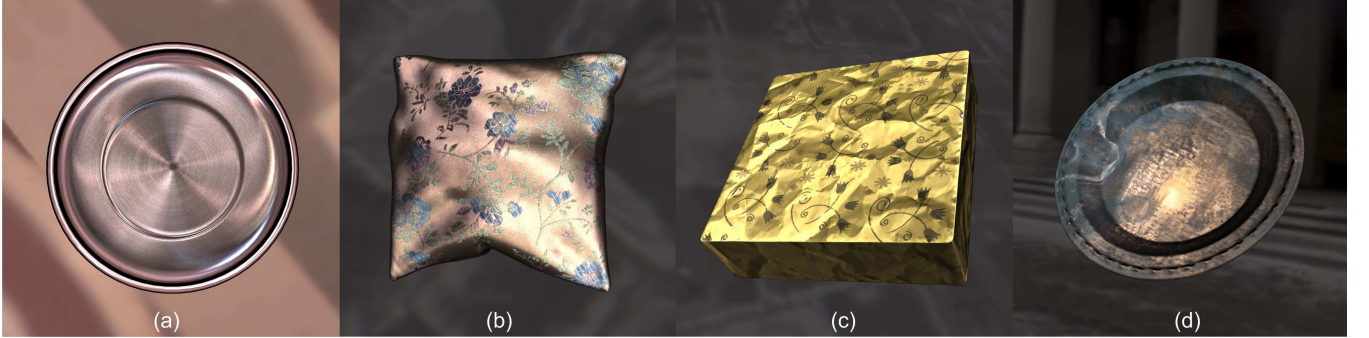[*]Tsinghua University   [†]Microsoft Research Asia   [‡]Microsoft Research

Figure 1: Renderings of high-resolution SVBRDFs reconstructed by our method from two-phase, low-dimensional captured data. (a) Anisotropic brushed metal. (b) Satin with complex needlework. (c) Wrinkled glossy paper. (d) Weathered copper.

Abstract

Manifold bootstrapping is a new method for data-driven modeling of real-world, spatially-varying reflectance, based on the idea that reflectance over a given material sample forms a low-dimensional manifold. It provides a high-resolution result in both the spatial and angular domains by decomposing reflectance measurement into two lower-dimensional phases. The first acquires *representatives* of high angular dimension but sampled sparsely over the surface, while the second acquires *keys* of low angular dimension but sampled densely over the surface.

We develop a hand-held, high-speed BRDF capturing device for phase one measurements. A condenser-based optical setup collects a dense hemisphere of rays emanating from a single point on the target sample as it is manually scanned over it, yielding 10 BRDF point measurements per second. The second phase captures N=20-200 images of the entire sample from a fixed view and lit by a varying area source. We show that the resulting N-dimensional keys capture much of the distance information in the original BRDF space, so that they effectively discriminate among representatives, though they lack sufficient angular detail to reconstruct the SVBRDF by themselves. At each surface position, a local linear combination of a small number of neighboring representatives is computed to match each key, yielding a high-resolution SVBRDF. A quick capture session (10-20 minutes) on simple devices yields results showing sharp and anisotropic specularity and rich spatial detail.

1 Introduction

Real-world materials exhibit rich and detailed reflectance variation, which must be modeled or acquired to produce realistic CG imagery. Surface reflectance is represented by the six-dimensional spatially varying bidirectional reflectance distribution function (SVBRDF) $\rho(\boldsymbol{x}, \mathbf{i}, \mathbf{o})$ [Nicodemus et al. 1977], describing how much radiance reflects at each surface point $\boldsymbol{x}$ when viewed from direction $\mathbf{o}$ and lit from direction $\mathbf{i}$. The parameter $\boldsymbol{x}$ represents the *spatial* domain component while $\mathbf{i} \times \mathbf{o}$ represents the *angular* domain component. Brute force capture requires hours of measurement and processing, using large, expensive hardware rigs. This impracticality of SVBRDF measurement greatly limits its use in CG applications.

Our goal is to simplify SVBRDF measurement by eliminating the collection of redundant data and doing the acquisition on sim-

ple, inexpensive devices. Several methods [Debevec et al. 2000; Gardner et al. 2003] attempt to do this by fitting a simple parametric model to the BRDF at each point using data taken from a sparse set of view and light directions. However, these models are generic, based on just a few parameters, and lack the power to capture real materials [Ngan et al. 2005]. Spatial redundancy has also been exploited to speed up SVBRDF acquisition, but previous methods again depend on ill-fitting parametric models [Lensch et al. 2003; Debevec et al. 2004; Goldman et al. 2005] or require dense sampling over both the spatial and angular domains to obtain a high-resolution result [Zickler et al. 2005; Weyrich 2006; Wang et al. 2008; Alldrin et al. 2008].

We propose *manifold bootstrapping* for modeling high-resolution surface reflectance from sparse captured data. We assume that spatial reflectance variation over a particular capture target forms a low-dimensional manifold in high-dimensional BRDF space. Manifolds are locally but not globally linear. More precisely, arbitrary linear combinations of points on the BRDF manifold do not generally lie on the manifold and instead generate implausible BRDFs [Matusik et al. 2003a]. On the other hand, linear combinations of nearby points provide a good approximation to the manifold's local structure, via *local linear embedding* [Roweis and Saul 2000].

These ideas let us to separate acquisition into two lower-dimensional phases. The first captures the BRDF manifold specialized to a given material while the second determines the precise position on that manifold occupied at each $\boldsymbol{x}$. Specifically, the first phase captures a set of *full-resolution BRDF representatives* (shortened to *representatives*), at scattered points on the surface whose location is ignored. The second phase captures a set of reflectance measurements densely over the surface but sparsely in the angular domain; specifically, under only a few different lighting conditions called the *key measurements*. This yields at each $\boldsymbol{x}$ a low-dimensional key vector, in which each component represents the material's appearance with respect to a different key measurement. For each $\boldsymbol{x}$, we reconstruct a high-resolution BRDF by computing a linear combination of *neighbor* representatives whose response to the key measurements matches the measured key at $\boldsymbol{x}$. A small number of key measurements suffices to roughly preserve distance in the high-dimensional BRDF space and determine how the BRDF manifold is spatially mapped.

Our method handles bumpy and anisotropic materials having spatially-varying normal and tangent vectors. To avoid unduly

lengthy scanning in phase one, we synthetically enlarge the representative set. For bumpy surfaces, we enlarge by applying a discrete series of normal tilts to each original representative. Similarly, for anisotropic surfaces we amplify based on discrete azimuthal rotations. We then bootstrap as before against the enlarged set.

Manifold bootstrapping is a new and general approach for acquiring complex, spatially-varying surface reflectance, including isotropic or anisotropic, and diffuse to highly specular materials. It simplifies SVBRDF acquisition by decomposing it into two novel phases. For phase one capture, we develop a portable device for microfacet BRDF acquisition. The device is based on a pair of condenser lenses and captures hundreds of representative points in a few minutes of scanning. For phase two capture, we obtain good results using a small number (20-200) of key measurements based on varying lighting and a fixed view. We develop a novel scaling method that handles non-orthogonal lighting variation, allowing area/environmental light sources that can be freely moved but need not be exactly controlled. We show that an area source provides better distance discrimination compared to impulsive lighting used in previous work. Overall, our approach provides a practical, inexpensive, and high-quality solution for on-site reflectance acquisition which we demonstrate on a set of real materials.

2 Related Work

2.1 Brute Force Acquisition

A set of spatial gonioreflectometers directly measures SVBRDFs [Dana et al. 1999; McAllister et al. 2002; Lawrence et al. 2006], BTFs [Dana 2001; Muller et al. 2005], and reflectance fields [Garg et al. 2006]. These methods densely sample the angular domain of view and light directions as well as the spatial domain. In all cases, special rigs are needed and the 6D datasets are huge and require hours to collect and process. Han et. al. [2003] developed a kaleidoscope-based compact device for quickly measuring BTFs. Although this device can be used for SVBRDF acquisition, the angular resolution is limited.

Image-based approaches [Marschner et al. 1999; Lu et al. 1998] capture a 4D BRDF from a convex object having spatially homogeneous reflectance. These methods ignore spatial variation. Recently, several devices [Mukaigawa et al. 2007; Moshe et al. 2008] have been proposed for fast BRDF measurement. Our phase one capture device is based on optical principles similar to those in [Mukaigawa et al. 2007], but is designed for quick scanning over different surface points.

2.2 Data Driven Modeling

Matusik et al. [2003a] investigate the dimensionality of BRDF space by analyzing more than 100 isotropic BRDFs. Wang et al. [2006] reconstruct the BRDF manifold from samples over the surface and from these predict reflectance variation over time. Lawrence et al. [2006] develop an automatic method to estimate a lower-dimensional BRDF basis from measured data, to simplify rendering and editing. None of these methods is designed for the acquisition problem itself and instead uses measured SVBRDF data as input for further compression or prediction.

Exploiting Angular Redundancy Gardner et al. [2003] scan the surface with a linear light source and capture its reflectance from a fixed view. An isotropic Ward model is then fit to the captured data at each point. Such a model is too weak to accurately capture angular variation of many real-world materials. By constraining the material to human skin, Debevec et al. [2000] capture SVBRDFs of the human face from a fixed view and dense lightings.

Single Pass Methods Another class of methods exploits coherence in both the angular and spatial domain components using a single data collection pass. Lensch et al. [2003] reconstruct SVBRDFs

of a real object of known geometry. BRDFs are grouped into a small set each fit using a Lafortune model basis, and reflectance at every point is represented as a linear combination over this basis. Goldman et al. [2005] use the same linear combination idea but with an isotropic Ward model as the BRDF basis, to reconstruct both an object's shape and its SVBRDF from sparse measurements. These methods capture spatial variation, but miss details in the BRDF's anisotropy, specularity, and other types of angular variation, because they merge angular information from different spatial samples. [Zickler et al. 2005] models the SVBRDF using six-dimensional radial basis functions. By assuming isotropic reflectance that varies smoothly over space, BRDF fitting at each point can exploit sparse reflectance data by using information from neighboring points. Our approach makes no assumptions about the material's spatial distribution, which in general may not be spatially smooth. Recently, Alldrin et. al. [2008] extend the linear combination idea using an isotropic bivariate function as the BRDF basis. It is not clear how to extend this method for modeling anisotropic SVBRDFs. [Wang et al. 2008] models anisotropic surface reflectance from data captured from a single view and dense lighting directions, based on the general microfacet model. Reconstruction involves merging data from surface points having similar reflectance properties (i.e., similar partial NDFs). The method requires dense measurements over both space and lighting direction.

In general, methods based on a single data collection pass can not avoid the need for huge datasets to capture both spatial and angular details of complicated reflectance. By acquiring data in two separate passes, the first for angular and the second for spatial variation, our method significantly reduces the data and thus time needed for capture.

Two Pass Methods Some recent methods perform a form of two-step bootstrapping. To obtain surface reflectance of large outdoor scenes, Debevec et al. [2004] measure a set of representative BRDFs from small regions of the scene using controlled lighting, as well as images of the entire scene under natural lighting. At each scene point, the Lambertian color is recovered and its BRDF is modeled as a linear combination of two representative BRDFs whose diffuse colors are most similar to the point's. This approach works well for the specific application targeted, but fails in general when surface points have similar diffuse colors but different specular reflectance. We generalize the concept of key measurement, as well as the bootstrapping procedure, to enable capture of a wide range of materials.

Matusik et al [2003b] represents an isotropic BRDF as a linear combination of 100 BRDFs chosen from an existing database. Based on this reconstruction, another BRDF can be optimally projected using about 800 measurements. Similarly, [Weyrich 2006] represents the reflectance of human skin as a linear combination of a set of isotropic BRDFs manually selected from an existing database. Weights for each surface point are computed via nonnegative matrix factorization (NMF), based on data that is densely acquired from 15 views and 300 light directions. Our approach handles both isotropic and anisotropic BRDFs. Most significantly, it measures many more representatives that are specialized to each particular sample, in order to further reduce by 1-2 orders of magnitude the spatially dense "key" measurements needed in its second phase. We also allow keys measured under area light sources with non-orthogonal variation.

Wang et al. [2009] propose an efficient two-pass method based on Kernel Nyström to acquire fixed-view light transport from sparse measurements and allow image relighting. This is a different and lower-dimensional problem than reflectance acquisition, which depends on both view and light directions. Lasers and precisely-controlled lighting are used for acquisition in a dedicated dark laboratory, while our goal is to acquire SVBRDFs without complex control of the light sources and environment. Most important, their
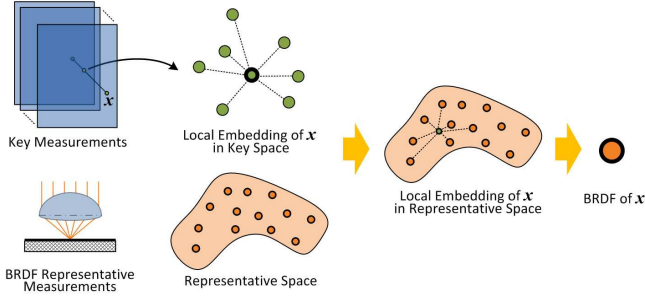
Figure 2: SVBRDF bootstrapping. A key vector at each spatial position x is projected to the space of matching vectors to determine a local linear embedding. The linear weights and neighborhood indices are then applied the full-resolution representatives to reconstruct the BRDF at x.

matrix reconstruction algorithm assumes global linearity of light transport and so is inappropriate for reconstructing the BRDF manifold.

3 SVBRDF Manifold Bootstrapping

This section introduces the basic theory of manifold bootstrapping for SVBRDF capture. Device setup and data acquisition are described in the next section.

3.1 Representative and Key Measurement

Representative Measurement In the first phase, we capture a set of M high-resolution representative BRDFs, indexed by p and denoted $B^* = \{b_p^*(\mathbf{o}, \mathbf{i}) \mid p = 1, 2, \dots M\}$. To represent BRDFs, each *representative vector*, $\boldsymbol{b}_p^*$, comprises $N_b = N_\mathbf{o} \times N_\mathbf{i}$ samples, $N_\mathbf{o}$ over viewing directions and $N_\mathbf{i}$ over lighting directions. We assume this set of representatives adequately samples the BRDF manifold across the surface.

To uniformly sample the BRDF manifold, we cull nearly identical representatives if their distance is less than ε, fixed at 10% of the average distance over all pairs of nearest neighbors.

Key Measurement The second phase measures a low-dimensional set of keys, or reflectance responses over the whole sample. Critical to bootstrapping is a set of key measurements that is still able to accurately discriminate BRDF features. Previous work [Lawrence et al. 2006; Wang et al. 2008] has shown that many BRDFs are well-characterized by a single 2D BRDF slice; i.e., by measurements with respect to varying lighting but a fixed view. This is because specular reflectance for many real-world materials can be represented using the *microfacet model* [Cook and Torrance 1982], which expresses a complex 4D BRDF in terms of a simpler, 2D normal distribution function (NDF). The NDF can then be inferred by measuring data which covers the hemisphere of *half-angle vectors* midway between view and light directions,

$$\mathbf{h} = (\mathbf{o}+\mathbf{i})/\|\mathbf{o}+\mathbf{i}\|. \tag{1}$$

This is clearly possible from measurements which vary the lighting but fix the view. The microfacet model will be used again and discussed in more detail in the next section. Note that the fact that real materials are captured by the microfacet model does not imply that they can be captured by simple parametric models: real-world NDFs are complicated and require tabulation or more sophisticated modeling [Ngan et al. 2005; Wang et al. 2008].

The view direction, $\mathbf{o}^*$, is chosen to be $45°$ from directly overhead. The provides the best coverage of half-angle vectors as the light source is varied.

Our key measurement captures N images of the material sample, each indexed by j and acquired from a fixed view direction $\mathbf{o}^*$

and under a known but varying source radiance field L_j. The measured reflectance responses at each point x provide constraints on integrals of the BRDF $b_x(\mathbf{i}, \mathbf{o})$, via

$$\boldsymbol{r}_j(\boldsymbol{x}) = \int_{\Omega_+(\mathbf{n})} b_{\boldsymbol{x}}(\mathbf{i}, \mathbf{o}^*)\,(\mathbf{n} \cdot \mathbf{i})\, L_j(\mathbf{i})\,\mathrm{d}\mathbf{i}, \tag{2}$$

where $\mathbf{n}$ is the surface normal and $\mathbf{o}^*$ and L_j are the view direction and source radiance fields for the j-th key measurement, respectively.

Assembling all N reflectance responses at surface point x into an N-dimensional *key vector*, $\boldsymbol{r}_{\boldsymbol{x}} = \left(r_1(\boldsymbol{x}), r_2(\boldsymbol{x}), \cdots, r_N(\boldsymbol{x})\right)^T$, we can represent (2) in matrix form as

$$\boldsymbol{r}_{\boldsymbol{x}} = \boldsymbol{R}\boldsymbol{b}_{\boldsymbol{x}}, \tag{3}$$

where $\boldsymbol{b}_{\boldsymbol{x}}$ is the BRDF vector at $\boldsymbol{x}$. The $N \times N_b$ *key measurement matrix*, $\boldsymbol{R}$, converts sampled BRDFs to key measurements and is given by

$$\boldsymbol{R}_{jk} = \begin{cases} (\mathbf{n} \cdot \mathbf{i}_{k_\mathbf{i}})\, L_j(\mathbf{i}_{k_\mathbf{i}}), & \mathbf{o}_{k_\mathbf{o}} = \mathbf{o}^* \\ 0, & \text{otherwise.} \end{cases} \tag{4}$$

The indices $k_\mathbf{o}$ and $k_\mathbf{i}$ decompose the overall index k of the packed BRDF vector $\boldsymbol{b}_{\boldsymbol{x}}$ into its constituent view and lighting directions, via $k = k_\mathbf{o} N_\mathbf{i} + k_\mathbf{i}$. In fact, the dimensionality of $\boldsymbol{R}$ is really only $N \times N_\mathbf{i}$ (not $N \times N_b$), because it is based on a single view and so has no response to view vectors other than $\mathbf{o}^*$.

3.2 Manifold Bootstrapping Overview

Given the previous two-phase measurement of a material sample, our method combines the two to reconstruct a high-resolution SVBRDF as shown in Figure 2.

Local BRDF Reconstruction Interpolation of distant BRDFs leads to implausible reflectance, as demonstrated in [Matusik et al. 2003a] for isotropic BRDFs of different (spatially homogeneous) materials. For anisotropic BRDFs, the problem is even worse (see Figure 10f). We solve this problem by bootstrapping using *local* reconstruction, which interpolates only over nearby representatives. We assume that the local dimensionality of the BRDF manifold is constant.

Mathematically, a particular BRDF $\boldsymbol{b}_{\boldsymbol{x}}$ at a spatial position x can be represented as a convex linear combination of a small number k of nearby representatives, called the *representative neighborhood*, $\boldsymbol{b}_p^*, p \in \delta(\boldsymbol{b}_{\boldsymbol{x}}), k = |\delta(\boldsymbol{b}_{\boldsymbol{x}})|$:

$$\boldsymbol{b}_{\boldsymbol{x}} \approx \sum_{p \in \delta(\boldsymbol{b}_{\boldsymbol{x}})} w_p \boldsymbol{b}_p^*, \qquad \sum_{p \in \delta(\boldsymbol{b}_{\boldsymbol{x}})} w_p = 1, \tag{5}$$

The neighborhood here is defined in terms of L2 distance in BRDF space, not spatial distance. This ensures that the linear combination produces a physically plausible result.

Representative Projection and Bootstrapping Substituting (5) into (3), we obtain a constrained linear equation on the weights w_p:

$$\boldsymbol{r}_{\boldsymbol{x}} = \sum_{p \in \delta(\boldsymbol{r}_{\boldsymbol{x}})} w_p \boldsymbol{r}_p^*, \qquad \sum_{p \in \delta(\boldsymbol{r}_{\boldsymbol{x}})} w_p = 1 \tag{6}$$

where

$$\boldsymbol{r}_p^* = \boldsymbol{R}\boldsymbol{b}_p^*. \tag{7}$$

The projection in (7) numerically applies the key lighting we captured in phase two to the representative BRDFs we captured in phase one, and also evaluates at the key viewing direction $\mathbf{o}^*$. It reduces an N_b-dimensional representative vector, $\boldsymbol{b}_p^*$, to an N-dimensional *matching vector*, $\boldsymbol{r}_p^*$. Equations (5) and (3) imply that

the measured key vector r_x can be represented as a linear combination of neighboring matching vectors, r_p^*, $p \in \delta(r_x)$.

Because we do not know the entire BRDF vector b_x but instead only the key vector r_x, we require that key vectors roughly preserve distance so that a neighborhood in key vector space corresponds to a similar neighborhood in the original BRDF space. This requires a sufficient number of key measurements.

3.3 Manifold Bootstrapping Details

Estimating Local BRDF Dimensionality We choose k based on an analysis of intrinsic local dimensionality of the representative set. The basic idea is to assemble a growing set of neighbors in terms of increasing distance around each representative, considered as a local center. We analyze dimensionality based on a singular value decomposition (SVD) of vector differences of all neighbors in the set to this center. Eliminating singular values less than a threshold (e.g. preserving 95% of total energy), the number of significant singular values remaining forms an estimate of dimensionality. At first, dimensionality increases rapidly, since each new neighbor typically adds an entire new dimension. But after we have discovered a spanning set of neighbors, additional ones add no more significant dimensions to the space. We use a simple heuristic that fixes dimensionality when twice as many neighbors fails to increase the dimensionality estimate. We then average local dimensionality estimates over a random selection of representative centers.

Uniform Measurement Scaling Overlapping light sources and varying environmental lighting in key measurement produce a non-orthogonal key measurement matrix. This leads to ellipsoidal rather than spherical neighborhoods in key space, and so complicates the selection of neighbors and distorts the interpolation. We orthogonalize the projection by applying the SVD to R, yielding

$$R = U_R \Lambda_R V_R \tag{8}$$

where U_R is an $N \times N$ orthogonal matrix of left-hand eigenvectors, Λ_R is an $N \times N$ diagonal matrix of eigenvalues, and V_R is an $N \times N_b$ (really $N \times N_i$) orthogonal matrix of transposes of right-hand eigenvectors. Λ_R should contain no zero or very small elements; if it does, then we are measuring redundant (i.e., linearly dependent) lighting configurations, which add no new information to the key.

To remove non-uniform scaling in our key measurements, we apply the SVD in (8) to obtain the *uniform key vector*

$$\hat{r}_x = \Lambda_R^{-1} U_R^T r_x. \tag{9}$$

We also define the *uniform matching vector* $\hat{r}_p^*$ as

$$\hat{r}_p^* = V_R b_p^*. \tag{10}$$

Neighbors can now be found in the uniform key space using a simple distance threshold over these N-dimensional vectors, in order to match a linear combination of the $\hat{r}_p^*$ to each $\hat{r}_x$.

Neighborhood Selection After uniform measurement scaling, the representative neighborhood δ is determined at each spatial position x by finding the k-nearest uniform matching vectors $\hat{r}_p^*$ to the uniform key $\hat{r}_x$. We use approximated nearest neighbor (ANN) search [Mount and Arya 1997] to accelerate finding the k-nearest neighbors. We also remove outliers having distance more than 5 times of the average distance over all neighborhoods.

Local Linear Combination We then determine the linear weights, w_p, based on the distance metric in each local neighborhood [Roweis and Saul 2000], via:

$$w_p = \sum_{q \in \delta(r_x)} C_{pq}^{-1} (\hat{r}_x \cdot \hat{r}_q^* + \lambda), \tag{11}$$

$$\lambda = \frac{1 - \sum_{p,q \in \delta(r_x)} C_{pq}^{-1} (\hat{r}_x \cdot \hat{r}_q^*)}{\sum_{p,q \in \delta(r_x)} C_{pq}^{-1}}. \tag{12}$$

$C_{pq} = \hat{r}_p^* \cdot \hat{r}_q^*$ denotes the covariance matrix of the neighborhood and C^{-1} is its inverse. We compute the inverse based on SVD, and clamp reciprocals of small singular values back to 0. Though negative weight solution are theoretically possible, in practice, we don't see negative weights.

3.4 Synthetic Enlargement for Representatives

To handle bumpy surfaces, we enlarge the representative set by rotating each BRDF to align the vertical direction to a discrete set of tilted normals. The set is regularly sampled using 120 azimuthal angles and 30 polar angles in a $75°$ range, yielding an enlargement factor of 3600. The same bootstrapping algorithm is then applied to capture spatially-varying bumpy reflectance. After enlargement, nearly identical representatives are removed using distance culling as described in Section 3.1.

For anisotropic materials, we similarly rotate the derived BRDF around the normal direction by a discrete set of 360 azimuthal angles and add the corresponding BRDFs to the example set. We can then recover the anisotropic reflectance and local orientation angle at each spatial position.

Given a 3×3 rotation matrix $\mathscr{R}$, the rotated BRDF $b'(\mathbf{i}, \mathbf{o})$ is given by

$$b'(\mathbf{i}, \mathbf{o}) = b(\mathscr{R}^T \mathbf{i}, \mathscr{R}^T \mathbf{o}). \tag{13}$$

To handle tilts due to normal variation, representative BRDFs are defined on the full spherical domain, not just the upper hemisphere. The lower hemisphere of the original BRDF b is zeroed out before rotation. In our implementation, since our phase one capture relies on the microfacet model, we can simply rotate the NDF's half-angle vector $\mathbf{h}$, and then convert the NDF to a full 4D BRDF (see Section 4.1).

3.5 Key Measurement Validation

Key measurements must adequately discriminate BRDF features in two ways. First, they should ensure that representative neighborhoods in "key" space, $\delta(r_x)$, also correspond to neighborhoods in BRDF space, $\delta(b_x)$, so that distant BDRFs are not interpolated. Second, they should ensure that local distances in the BRDF manifold are preserved, to yield an accurate local reconstruction. This motivates an investigation of how well key measurements preserve distance in the original BRDF manifold, at both small and large length scales.

Overall distance preservation τ over a neighborhood of representatives of radius r, $\delta(p, r) = \{q \mid ||b_p^* - b_q^*|| < r\}$ can be measured by:

$$\tau(p, r) = \frac{\sum_{i,j \in \delta(p,r)} ||\hat{r}_i^* - \hat{r}_j^*||}{\sum_{i,j \in \delta(p,r)} ||b_i^* - b_j^*||}. \tag{14}$$

In the uniformly-scaled space, we have $0 \le ||\hat{r}_i^* - \hat{r}_j^*|| \le ||b_i^* - b_j^*||$. The closer τ is to 1, the better our key measurement is at discriminating between representatives in the neighborhood. Based on this, we examine average distance preservation at various length scales, r via

$$\bar{\tau}(r) = 1/M \sum_{p=1}^{M} \tau(\delta(p, r)). \tag{15}$$

Finally, we define *global distance preservation*,

$$\tau_g = \bar{\tau}(\infty) \tag{16}$$

by calculating average distance over all pairs of representatives. We also define *local distance preservation*

$$\tau_l = \bar{\tau}(\bar{r}) \tag{17}$$

where $\bar{r}$ is the average local radius over all representative BRDFs. It is defined as the max distance over the k nearest neighbors to each representative, averaged over all representatives.
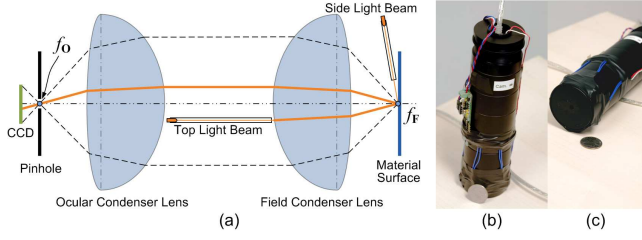
Figure 3: Single point BRDF measurement device (phase 1): (a) optical design, (b/c) prototype from side/bottom view.

4 SVBRDF Data Acquisition

Our approach captures two datasets from a flat sample of the target material. Typical sample dimensions are 10cm×10cm. Our device setups are portable and handle natural background lighting and inexact lighting control, allowing materials to be captured onsite without the need to move them to a dedicated capture room.

4.1 Acquiring Representatives: BRDF Samples

We have developed a portable device for capturing a hemispherical field of reflected rays emanating from a single point on the material sample using a single camera position. Data is acquired by illuminating the surface point using $n_l = 6$ lighting directions and capturing its resulting reflectance. A high-resolution general microfacet BRDF [Ashikhmin et al. 2000] is derived from this captured data. We scan the sample to acquire about typically hundreds of BRDFs scattered over its surface.

Device Setup Figure 3 shows the design of our single-point BRDF measurement device. Our setup includes a pair of Anchor Optics 47mm condenser lenses with 21mm focus length, a 200μm pinhole and a Firefly[R] MV camera from Point Grey Research. These components are mounted along the same optical axis using a lens tube from Thorlabs. We use six high-brightness LEDs as light sources; each is attached to a carbon fiber tube to generate a light beam. One (top light beam) is mounted between the two condenser lenses and illuminates the capturing point at roughly a 10 degree bias from the vertical direction. The other five (side light beams) are mounted around the optical axis between the field condenser lens and the target surface, and illuminate the capturing point at 20 degrees above the horizontal plane.

A sample is placed at the focal plane of the field condenser lens, f_F. The pinhole is placed at the focal plane of the ocular condenser lens, f_O, and images the light field at a single point on the target surface onto a video camera. The acceptance angle of the condenser lens is 48° from the optical axis. The camera communicates with a laptop via an IEEE1394 cable, which also supplies power for the LEDs and their control unit. A housing ensures the device is at the correct distance from the target sample.

Calibration The lens tube ensures optic alignment of the lenses, pinhole and camera. Distances between them are manually adjusted. The LED for the top light beam is held by an acrylic disc; its position is calibrated by measuring a mirror. Positions of the side LEDs are calibrated in manufacture. We calibrate the color and intensity of each LED by measuring a color checker pattern. Radial distortion of the dual condenser system is analytically calculated based on the specification from Anchor Optics, and determines the view direction at each pixel in the captured image.

Capturing The device is a cylinder 50mm in diameter and 150mm tall, and weighs around 500g. We scan it over the sample to collect BRDFs at different locations. For each position, we acquire six images lit by each LED and two images per light for exposure bracketing. The camera captures images of resolution 320×240 at 135Hz, yielding around 0.1s per BRDF point capture. In a postprocess, each exposure pair is merged into an HDR image [Debevec
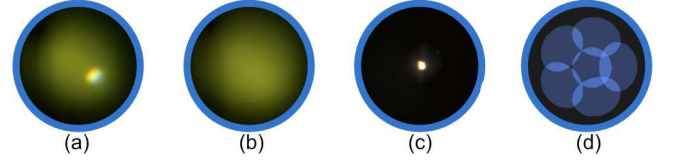

Figure 4: NDF reconstruction: (a) 2D BRDF slice captured using top light beam, (b) using side light beam, (c) reconstructed NDF, (d) covered region in the reconstructed NDF. BRDF slices from these six lighting directions cover most of the NDF domain.

and Malik 1997], and the resulting 6 images of 240×240 used to derive a high-resolution BRDF. Figure 4a shows an example.

The top light LED component occludes a 3mm diameter hole in the captured image. Since the top light beam is biased from the optic axis, this hole typically does not occlude the peak of the specular lobe. We obtain the occlusion mask when calibrating with the color checker. If the hole contains no high frequency features, we fill it with harmonic interpolation [Schuster 2001]. We detect this by querying the intensity range of pixels surrounding the hole and testing whether the max/min ratio exceeds 2. In that case, we discard the sample.

Reflectance samples are then computed from the six HDR images by dividing by the cosine factor and light intensity

$$\rho\left(\mathbf{o}(\boldsymbol{u}), \mathbf{i}_l\right) = \frac{G_l(\boldsymbol{u})}{(\mathbf{n} \cdot \mathbf{i}_l) L_l} \tag{18}$$

where $\boldsymbol{u}$ is the pixel position in the image corresponding to the view direction $\mathbf{o}(\boldsymbol{u})$, and $\mathbf{i}_l$ and L_l are the direction and intensity of the l-th LED. These quantities are all determined in calibration.

In sustained mode, we move the device continuously but slowly (e.g. around 1mm/s) over materials with smooth spatial variation. For materials with piecewise reflectance discontinuities or small details, the device also runs in a triggering mode. Placing the device on the desired target location, the user triggers a single BRDF point capture using a UI on the computer connected to the device.

Reconstruction To reconstruct a high-resolution 4D BRDF from this captured data, we decompose the BRDF into diffuse and specular components. The diffuse component ρ_d is determined by using a simple minimum filter on the samples ρ in (18), via

$$\rho_d = \frac{\sum_l \min_{\boldsymbol{u}} \{\rho(\mathbf{o}(\boldsymbol{u}), \mathbf{i}_l)\}}{n_l}. \tag{19}$$

The specular component is the residual after subtracting this diffuse term:

$$\rho_s\left(\mathbf{o}(\boldsymbol{u}), \mathbf{i}_l\right) = \rho\left(\mathbf{o}(\boldsymbol{u}), \mathbf{i}_l\right) - \rho_d. \tag{20}$$

We then represent the specular component with a general microfacet model [Ashikhmin et al. 2000] as

$$\rho_s(\mathbf{o}, \mathbf{i}) = c_s \frac{D(\mathbf{h}) S(\mathbf{i}) S(\mathbf{o}) F(\mathbf{o}, \mathbf{i})}{\pi (\mathbf{i} \cdot \mathbf{n}) (\mathbf{o} \cdot \mathbf{n})}, \tag{21}$$

This model is defined in terms of five factors: a microfacet normal distribution function (NDF) D in terms of the half-angle vector from (1), its shadowing factor S, a Fresnel reflection factor F, and the scalar specular coefficient, c_s. We assume the surface normal is aligned to the z axis: $\mathbf{n} = \mathbf{z} = (0, 0, 1)$. Since D dominates the other factors in determining the high-frequency characteristics of BRDF, we follow [Ashikhmin et al. 2000; Debevec et al. 2000; Wang et al. 2008] and tabulate it as a square image using the spherical parameterization in [Shirley and Chiu 1997]. We fit this microfacet BRDF in (21) from the measured specular data ρ_s in (20) using the method described in [Ngan et al. 2005]. In our case, the view direction varies densely rather than the lighting direction. Therefore we reconstruct the full NDF from partial NDFs inferred using a
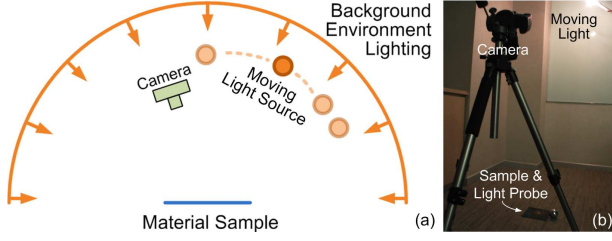
Figure 5: Device setup for capturing reflectance maps (phase 2): (a) diagram, (b) photograph.

sparse set of n_l lighting directions. We represent the recovered NDF by a 400×400 square image using the spherical parameterization in [Shirley and Chiu 1997]. Figure 4 summarizes the process and shows an example.

4.2 Acquiring Keys: Reflectance Maps

Keys are based on reflectance maps captured from a single view and lit by N different lighting configurations (Figure 5). The lighting can include variable environmental/area sources and their inter-reflection off surrounding geometry, as shown in Figure 6. The light source is attached to a hand-held pole and moved in a 2D plane opposite the sample from the camera, about 1.5m away from the sample center. We attempt to uniformly sample this plane, and ensure that the set of reflected directions are "covered" by a light direction (i.e., make a highlight appear on the sample). Precise lighting control is not necessary.

A mirror ball is used to probe the lighting applied. A Canon 30D camera with EF-100 2.8 lens is placed above and 2.0m away from the center of the material sample. Image resolution is 3504×2336.

Before capturing, we calibrate the camera's position and orientation using the method in [Zhang 2000]. For each lighting change, we record an HDR image including the material and the mirror ball using exposure bracketing as in [Debevec and Malik 1997]. In our prototype system, we simply move the light source around the sample by hand.

The process is finished after capturing N images, resulting in the material's reflectance responses, $r_j(\boldsymbol{x})$, and reconstructed source radiance fields, $L_j(\mathbf{i})$, for $j \in 1, 2, \ldots, N$. The environmental lighting and moving area light source is far enough away to reasonably assume that the radiance field is constant over the entire material sample. We also compute the viewing direction $\mathbf{o}^\star$ at the sample center and assume it is constant over all $\boldsymbol{x}$ as well.

Key Lighting Dimensionality To investigate the sufficiency of key lighting measurements, we captured 100 lighting conditions based on a small varying area light source, and randomly selected N as input to generate the matching vector space of 1200 BRDFs, sampled from the example in Figure 11b. Results are averaged over 10 trials of this random lighting selection. Figure 7a plots distance preservation as a function of N. Global and local distance preservation converge fairly quickly as N increases. In our experiments, convincing results are obtained with $\tau_g > 0.9$ and $\tau_l > 0.85$. Evaluating τ_l and τ_g at a few hundred representatives takes little time and indicates whether our lighting configuration and value for N are sufficient. So this validation can be applied between phase one and before phase two, to guide the key measurement.
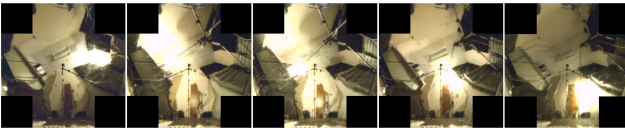

Figure 6: Lighting used for key measurement, L_j, visualized as hemicube maps.
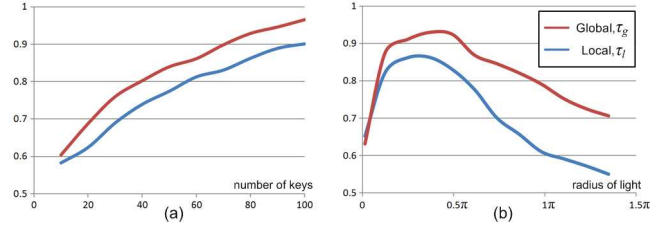

Figure 7: Distance preservation from representative space to matching vector space. (a) with increasing number of key measurements. (b) with increasing size of light source. Light radius is a linear angle, measured in radians. The materials used in this experiment is glossy ppaer, shown in Figure 11b. The distance preservations are computed from equations 16 and 17

Material Sample	Reflectance Maps		Representative BRDFs		
	Resolution	# (N)	# (M)	τ_g / τ_l	k
glossy paper (fig.11b)	1000×1000	50	30	0.90/0.87	10
wrinkle paper (fig.1c)	1000×600	200	30 †	0.90/0.83	13
weathered copper (fig.1d)	2000×2000	80	1200	0.93/0.85	21
aluminum pan (fig.1a)	2000×2000	200	10 §	0.99/0.85	15
satin (fig.1b)	2000×2000	90	30	0.99/0.85	15
wrinkled satin (fig.14)	1500×1500	200	30 †§	0.91/0.85	19

Table 1: Statistics for our examples. The M column shows number of representatives before enlargement. Materials using synthetic enlargement are marked with † for normal and § for tangent enlargement.

Key Lighting Size In addition to the number of measurements, the size of the light source used also affects the sufficiency of our key measurement. To investigate this parameter, we performed an experiment on the material shown in Figure 11b, which mixes BRDFs of different specularity and color. We synthetically generated a series of matching vectors with a moving disk-shaped light source of varying radius. We then plot local and global distance preservation as a function of light source size. The result is shown in Figure 7b. Smaller light sources generate a higher-rank projection V_R from (10). However, their corresponding key space is also sparsely supported, so significant variation in BRDF manifold can fall into its null space. Light sources of medium extent (e.g. 0.4π) provide the optimal balance between subspace dimensionality and wideness of support, and so best preserve distance.

5 Experimental Results

We implemented our SVBRDF bootstrapping algorithm on a Intel Core(TM)2 Duo 2.13G PC with 2G memory. Core capturing for BRDF representatives and reflectance map keys takes 10-20 minutes, excluding time for setting up the material target, camera, and light source. Subsequent data processing takes less than 10 minutes. Table 1 lists the parameters used in capturing. We infer 2D NDFs of resolution 400×400, yielding 4D BRDFs with more than ten million angular samples in viewing and lighting direction. The spatial resolution ranges from one to four million samples.

5.1 Method Validation

Test on Fully-Sampled SVBRDF We tested our bootstrapping method on fully sampled anisotropic SVBRDF data (greeting card from [Lawrence et al. 2006]). The experiment selected 1000 BRDFs from random positions as the representatives. Reflectance map capture was simulated by applying the Grace Cathedral environment map [Debevec and Malik 1997] along with a disk light source with angular radius 0.4π at a controlled direction. We then measured reconstruction error of our bootstrapping method as a function of the number N of different key measurements (light directions). For each N, we average over 10 randomly generated sets of light directions. Figure 8a shows average reconstruction error, which falls quickly as N increases. The right two columns of the
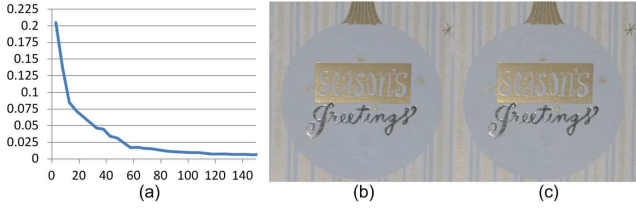
Figure 8: Validation example. (a) Reconstruction error as a function of number of lighting measurements, N. (b) Rendering with original SVBRDF. (c) Rendering with reconstructed SVBRDF.

figure compare rendered results between the original data (b) and our reconstructed SVBRDF (c), at a view not used in the second phase capture. An accurate match is obtained.

Comparison with Microfacet Synthesis We compared our method with microfacet synthesis [Wang et al. 2008]. Results are shown in Figure 9. We made $N=20 \times 20$ lighting measurements for microfacet synthesis, as suggested in [Wang et al. 2008], requiring capture of 400 reflectance images. Our method was based on $N=50$ key measurements. Both methods applied point source lighting. Even with such a large data set, microfacet synthesis generates results with grid artifacts on highly specular texels. The artifacts are caused by point light source sampling, which aliases specular peaks. By reconstructing based on full-resolution BRDFs acquired in a separate step, our method is able to avoid such artifacts with a greatly reduced measurement.

Effect of Neighborhood Size We also investigated how k affects reconstruction quality. Our experiment is based on the brushed aluminum sample with $N=100$ key measurements. We used representative set enlargement based on tangent rotation as described in Section 3.4. Using a total of $M=3600$ representatives, we compared reconstruction error from local linear combination as k varied from 1 to 3600. Results at a typical texel (marked with a red circle) are shown in Figure 10a. The ground truth BRDF is acquired at that point by the device described in Section 4.1. As expected, increasing k always reduces the fitting error between the key vector and the linear combination of matching vectors. When $k = N$, the number of parameters matches the number of constraints and the error drops to 0. This does not imply a corresponding reduction in error for the final BRDF, because reconstruction is based on a sparse key measurement and so becomes extremely under-determined. As discussed, the BRDF manifold is not globally linear so such under-determined linear combinations generate results off the BRDF manifold and provide a poor fit. Very large k thus generate an implausible BRDF with ghosting artifacts and high error, as shown in Figure 10ef. Over a broad range (4-60), the choice of k has little effect on reconstruction quality.

5.2 SVBRDF Capture Results

Figure 11 shows results for different material samples. We compare the rendered result of our reconstructed SVBRDFs to photographs of the captured sample with the same lighting conditions. Materials with smooth (a/d) and sharp (b/e) spatial variation are both handled. The left two columns show isotropic materials, while the rightmost shows anisotropic satin. The comparsion is made under

Figure 9: Comparison with result by microfacet synthesis [Wang et al. 2008]. (a) ground truth. (b) our result. (c) result of microfacet synthesis
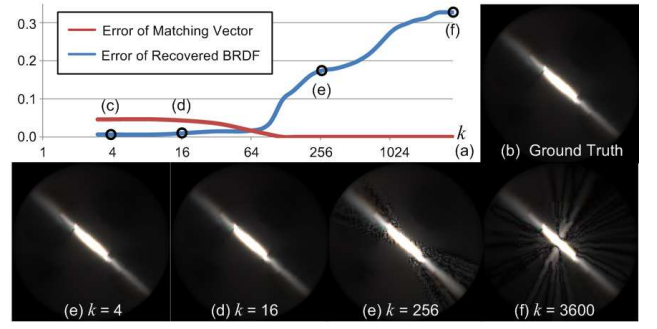

Figure 10: Local linear reconstruction with different neighborhood sizes, k. Error is measured by sum of squared differences (squared L2), normalized to the signal's sum of squares. BRDFs are visualized as 2D NDFs inferred from the microfacet model. (a) Matching vector and final BRDF reconstruction error vs. k. (b) BRDF ground truth. (c-f) reconstructed BRDF with different k, as marked in (a).

a novel view and light which does not correspond to any view or light conditions used in capture.

Figure 12 shows results for a bumpy isotropic material (b), an anisotropic material with spatially varying tangent (a), and a material with both both spatially-varying normals and tangents (c). Rendering results with reconstructed SVBRDFs match well with the ground truth, as shown in the second row. The number of representatives before enlargement is listed in Table 1. The wrinkled satin example enlarges based on both normal and tangent rotation; we reduced its enlargement factors to $72\times$ for tangent and $400\times$ for normal rotations, yielding 864k total representatives after enlargement. All other examples use $3600\times$ for normal and $360\times$ for tangent enlargement, as mentioned in Section 3.4. The figure also shows normal/tangent maps inferred by applying the same linear combination used to reconstruct each SVBRDF texel to the representative normal/tangent vectors themselves. Such vectors provide a good, low-dimensional proxy to visualize our method's output.

Figure 1 and 13 show rendered results of the acquired SVBRDFs mapped on objects, from two different views. A brushed aluminum pan is shown in (a); the fan-shaped highlight and detailed brushing pattern create a realistic appearance. A satin pillow with complex needlework is rendered with environment lighting in (b), and exhibits complex appearance changes as the view and light varies. Wrinkled glossy paper with sharp reflectance changes is rendered in (c). Progressively changing reflectance captured from a weathered copper plate is shown in (d). Figure 14 shows rendered results from the wrinkled satin SVBRDF capture. Refer to the accompanying
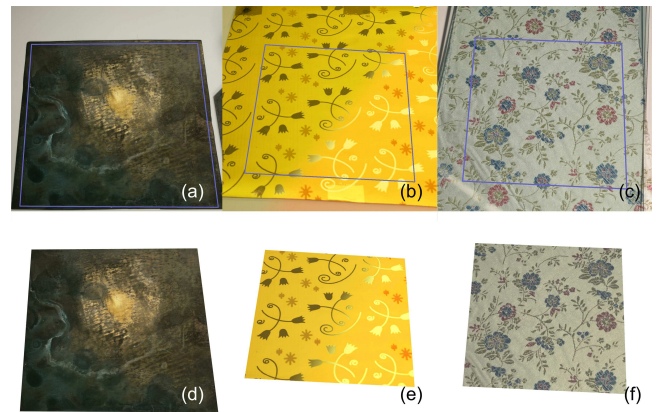

Figure 11: SVBRDF examples. Top row shows an original image of the example; bottom row shows the reconstructed SVBRDF rendered with the same lighting condition. Examples: (a/d) weathered copper plate, (b/e) glossy paper, (c/f) satin.
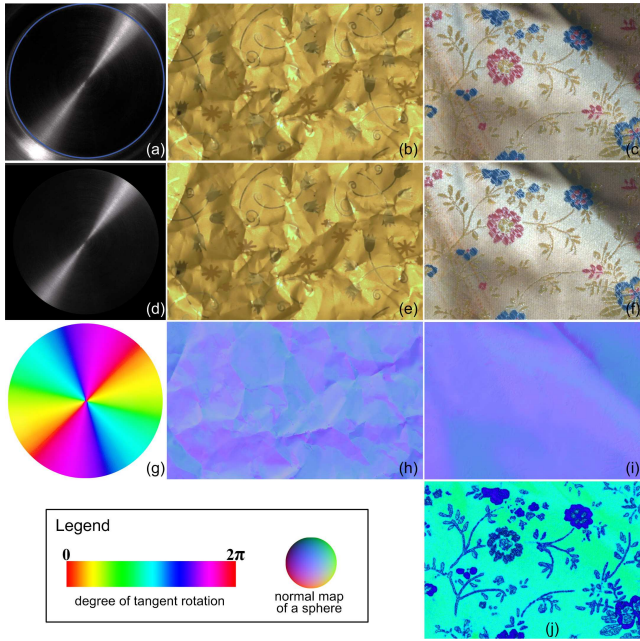
Figure 12: Enlarged SVBRDF examples. Top row shows an original image of the example, second row shows reconstructed SVBRDF rendered with the same lighting condition. Third and fourth rows show inferred normal and tangent maps. Examples: (a/d) brushed aluminum pan, (b/e) wrinkled glossy paper, (c/f) wrinkled satin. Image (g) shows the tangent map of (a); (h) shows the normal map of (b); (i/j) shows the normal/tangent map of (c).

video for further results of captured SVBRDFs.

6 Conclusion

Manifold bootstrapping simplifies and accelerates the capture of complex reflectance by decomposing data acquisition into two phases. One captures the overall BRDF manifold while the other maps this manifold over the surface. Both phases make only sparse measurements of the overall 6D SVBRDF. We propose a new compact device based on a pair of condenser lenses to scan BRDF point samples in the first phase. Using local linear embedding and representative set enlargement, we produce SVBRDFs of high resolution in both the spatial and angular domains from this sparse data. Captured materials exhibit convincing realism, isotropic and anisotropic specularity, and spatial detail.

Our method is general and may have application to other sorts of data capture, whenever representatives form a low-dimensional manifold in a high-dimensional space. It can also accommodate different methods for phase one and phase two measurement. Our hand-held BRDF scanner measures only a few light directions, and so requires amplification via the (single-bounce) microfacet model. Though this model has wide applicability [Ashikhmin et al. 2000; Wang et al. 2008], it does prohibit anomalous materials such as retro-reflective ones. Our method for acquiring reflectance maps is limited to flat surfaces without significant self-shadowing and self-masking. We would like to address these drawbacks in future work.

References

ALLDRIN, N., ZICKLER, T. E., AND KRIEGMAN, D. 2008. Photometric stereo with non-parametric and spatially-varying reflectance. In *CVPR*, 1–8.

ASHIKHMIN, M., PREMOZE, S., AND SHIRLEY, P. 2000. A microfacet-based BRDF generator. In *Siggraph 2000, Computer Graphics Proceedings*, ACM Press / ACM SIGGRAPH / Addison Wesley Longman, 65–74.
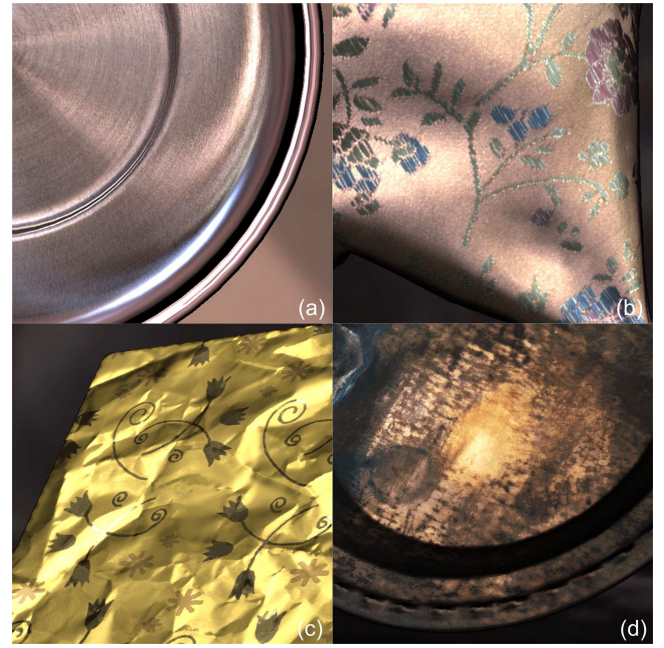
Figure 13: Zoomed up results: (a) brushed aluminum, (b) satin, (c) wrinkled glossy paper, (d) weathered copper.

COOK, R. L., AND TORRANCE, K. E. 1982. A reflectance model for computer graphics. *ACM Trans. Graph. 1*, 1, 7–24.

DANA, K. J., NAYAR, S. K., VAN GINNEKEN, B., AND KOENDERINK, J. J. 1999. Reflectance and texture of real-world surfaces. *ACM Transactions on Graphics 18*, 1, 1–34.

DANA, K. J. 2001. BRDF/BTF measurement device. In *Proceedings of eighth IEEE international conference on computer vision (ICCV)*, vol. 2, 460–466.

DEBEVEC, P. E., AND MALIK, J. 1997. Recovering high dynamic range radiance maps from photographs. In *ACM SIGGRAPH*, 369–378.

DEBEVEC, P., HAWKINS, T., TCHOU, C., DUIKER, H.-P., SAROKIN, W., AND SAGAR, M. 2000. Acquiring the reflectance field of a human face. In *Proc. SIGGRAPH 2000*, 145–156.

DEBEVEC, P., TCHOU, C., GARDNER, A., HAWKINS, T., POULLIS, C., STUMPFEL, J., JONES, A., YUN, N., EINARSSON, P., LUNDGREN, T., FAJARDO, M., AND MARTINEZ, P. 2004. Estimating surface reflectance properties of a complex scene under captured natural illumination. Technical report ICT-TR-06, University of Southern California Institute for Creative Technologies Graphics Laboratory.

GARDNER, A., TCHOU, C., HAWKINS, T., AND DEBEVEC, P. 2003. Linear light source reflectometry. *ACM Trans. Graph. 22*, 3, 749–758.

Figure 14: Rendering results for wrinkled satin.

GARG, G., TALVALA, E.-V., LEVOY, M., AND LENSCH, H. P. A. 2006. Symmetric photography: exploiting data-sparseness in reflectance fields. In *Eurographics Workshop/ Symposium on Rendering*, Eurographics Association, Nicosia, Cyprus, 251–262.

GOLDMAN, D. B., CURLESS, B., HERTZMANN, A., AND SEITZ, S. M. 2005. Shape and spatially-varying BRDFs from photometric stereo. In *International Conference on Computer Vision*, I: 341–348.

HAN, J. Y., AND PERLIN, K. 2003. Measuring bidirectional texture reflectance with a kaleidoscope. *ACM Trans. Graph. 22*, 3, 741–748.

LAWRENCE, J., BEN-ARTZI, A., DECORO, C., MATUSIK, W., PFISTER, H., RAMAMOORTHI, R., AND RUSINKIEWICZ, S. 2006. Inverse shade trees for non-parametric material representation and editing. *ACM Transactions on Graphics (Proc. SIGGRAPH) 25*, 3 (July).

LENSCH, H. P. A., KAUTZ, J., GOESELE, M., HEIDRICH, W., AND SEIDEL, H.-P. 2003. Image-based reconstruction of spatial appearance and geometric detail. *ACM Transaction on Graphics 22*, 2 (Apr.), 234–257.

LU, R., KOENDERINK, J. J., AND KAPPERS, A. M. L. 1998. Optical properties bidirectional reflectance distribution functions of velvet. *Applied Optics 37*, 25 (Sept.), 5974–5984.

MARSCHNER, S., WESTIN, S., LAFORTUNE, E., TORRANCE, K., AND GREENBERG, D. 1999. Image-based BRDF measurement including human skin. In *10th Eurographics Rendering Workshop*.

MATUSIK, W., PFISTER, H., BRAND, M., AND MCMILLAN, L. 2003. A data-driven reflectance model. *ACM Trans. Graph. 22*, 3, 759–769.

MATUSIK, W., PFISTER, H., BRAND, M., AND MCMILLAN, L. 2003. Efficient isotropic BRDF measurement. In *EGRW '03: Proceedings of the 14th Eurographics workshop on Rendering*, Eurographics Association, Aire-la-Ville, Switzerland, Switzerland, 241–247.

MCALLISTER, D. K., LASTRA, A. A., AND HEIDRICH, W. 2002. Efficient rendering of spatial bi-directional reflectance distribution functions. In *Proceedings of the 17th Eurographics/SIGGRAPH workshop on graphics hardware (EGGH-02)*, ACM Press, New York, S. N. Spencer, Ed., 79–88.

MOSHE, B.-E., WANG, J., BENNETT, W., LI, X., AND MA, L. 2008. An LED-only BRDF measurement device. In *Computer Vision and Pattern Recognition, 2008. CVPR 2008. IEEE Conference on*, 1–8.

MOUNT, D., AND ARYA, S. 1997. Ann: A library for approximate nearest neighbor searching. In *CGC 2nd Annual Fall Workshop on Computational Geometry*.

MUKAIGAWA, Y., SUMINO, K., AND YAGI, Y. 2007. High-speed measurement of BRDF using an ellipsoidal mirror and a projector. In *Computer Vision and Pattern Recognition, 2007. CVPR '07. IEEE Conference on*, 1–8.

MULLER, G., MESETH, J., SATTLER, M., SARLETTE, R., AND KLEIN, R. 2005. Acquisition, synthesis, and rendering of bidirectional texture functions. *Computer Graphics Forum 24*, 1, 83–109.

NGAN, A., DURAND, F., AND MATUSIK, W. 2005. Experimental analysis of BRDF models. *Eurographics Symposium on Rendering 2005*.

NICODEMUS, F. E., RICHMOND, J. C., HSIA, J. J., GINSBERG, I. W., AND LIMPERIS, T. 1977. Geometric considerations and nomenclature for reflectance. *Monograph 161,National Bureau of Standards (US)*.

ROWEIS, S. T., AND SAUL, L. K. 2000. Nonlinear dimensionality reduction by locally linear embedding. In *Science*, 2323–2326.

SCHUSTER, W. 2001. Harmonische interpolation. In *Math. Semesterber*, Springer-Verlag, 1–27.

SHIRLEY, P., AND CHIU, K. 1997. A low distortion map between disk and square. *J. Graph. Tools 2*, 3, 45–52.

WANG, J., TONG, X., LIN, S., PAN, M., WANG, C., BAO, H., GUO, B., AND SHUM, H.-Y. 2006. Appearance manifolds for modeling time-variant appearance of materials. *ACM Trans. Graph. 25*, 3, 754–761.

WANG, J., ZHAO, S., TONG, X., SNYDER, J., AND GUO, B. 2008. Modeling anisotropic surface reflectance with example-based microfacet synthesis. In *SIGGRAPH '08: ACM SIGGRAPH 2008 papers*, ACM, New York, NY, USA, 1–9.

WANG, J., DONG, Y., TONG, X., LIN, Z., AND GUO, B. 2009. Kernel nyström method for light transport. *ACM Trans. Graph. 28*, 3, 29:1–29:10.

WEYRICH, T. 2006. Acquisition of human faces using a measurement-based skin reflectance model.

ZHANG, Z. 2000. A flexible new technique for camera calibration. In *Pattern Analysis and Machine Intelligence, IEEE Transactions on*, vol. 22, 1330– 1334.

ZICKLER, T., ENRIQUE, S., RAMAMOORTHI, R., AND BELHUMEUR, P. 2005. Reflectance sharing: image-based rendering from a sparse set of images. In *Eurographics Symposium on Rendering*, Eurographics Association, Konstanz, Germany, K. Bala and P. Dutré, Eds., 253–264.